Journal of Magnetic Resonance **148,** 367–378 (2001)
doi:10.1006/jmre.2000.2263, available online at http://www.idealibrary.com on IDEAL®

Diffusion and Relaxation Effects in General Stray Field NMR Experiments

M. D. Hürlimann

Schlumberger-Doll Research, Ridgefield, Connecticut 06877-4108

Received July 31, 2000; revised November 16, 2000

We analyze the evolution of magnetization following any series of radiofrequency pulses in strongly inhomogeneous fields, with particular attention to diffusion and relaxation effects. When the inhomogeneity of the static magnetic field approaches or exceeds the strength of the RF field, the magnetization has contributions from different coherence pathways. The diffusion or relaxation induced decay of the signal amplitude is in general nonexponential, even if the sample has single relaxation times T_1, T_2 and a single diffusion coefficient D. In addition, the shape of the echo depends on diffusion and relaxation. It is possible to separate contributions from different coherence pathways by phase cycling of the RF pulses. The general analysis is tested on stray field measurements using two different pulse sequences. We find excellent agreement between measurements and calculations. The inversion recovery sequence is used to study the relaxation effects. We demonstrate two different approaches of data analysis to extract the relaxation time T_1. Finite pulse width effects on the timing of the echo formation are also studied. Diffusion effects are analyzed using the Carr–Purcell–Meiboom–Gill sequence. In a stray field of a constant gradient g, we find that unrestricted diffusion leads to nonexponential signal decay versus echo number N, but within experimental error the diffusion attenuation is still only a function of $g^2Dt_E^3N$, where t_E is the echo spacing.

Key Words: **stray field NMR; relaxation; diffusion; CPMG.**

1. INTRODUCTION

Recently, several new NMR applications have been developed that operate in grossly inhomogeneous fields. In stray field NMR (*1*), the static field is deliberately made very inhomogeneous to increase the sensitivity to diffusion (*2, 3*) and to enable high-resolution profiling. In the application of "inside-out" NMR measurements, the sample is outside the apparatus and large inhomogeneities are unavoidable. Such devices have been developed for well logging (*4*) and for materials testing (*5*).

In all these cases, the signal bandwidth is determined by the excitation bandwidth rather than the field inhomogeneities or sample properties. All pulses act as slice selective pulses and off-resonance effects become important. In this paper, we present a general analysis that is valid for any multipulse sequence in RF and static fields of arbitrary homogeneity and that fully treats diffusion and relaxation effects. The theory presented in Section 2 follows Kaiser *et al.* (*6*) and decomposes the signal into the contributions from different coherence pathways. This treatment makes it easy to design phase cycling schemes that select particular pathways. General expressions are given to calculate the spectrum, relaxation, and diffusion decay for each pathway and for the total signal.

The theoretical approach is tested by analyzing two different pulse sequences and comparing calculations with experimental results. In Section 4, the inversion recovery sequence is studied to focus on relaxation effects. In Section 5, the case of the Carr–Purcell–Meiboom–Gill (CPMG) sequence is analyzed with special attention to diffusion effects.

Our theoretical treatment can be viewed as an extension of earlier work by Sodickson and Cory (*7*). They formulated the problem in terms that are most convenient for imaging applications with time varying gradient pulses. Benson and McDonald (*8*) analyzed the specific case of the spin echo in a gradient field, but did not consider relaxation or diffusion effects. Goelman and Prammer (*9*) studied the CPMG sequence in a strong gradient and have given expressions for the first three echoes. In a recent paper (*10*), we have obtained simple asymptotic expressions for the CPMG echoes in terms of the eigenvectors of the refocusing cycle. The treatment included relaxation effects but not diffusion effects, except for the first two echoes.

2. THEORY

2.1. General Spin Dynamics in the Absence of Diffusion and Relaxation

For the calculation of the spin dynamics in inhomogeneous fields, we define two frequencies, $\Delta\omega_0$ and ω_1. $\Delta\omega_0$ is the offset of the local Larmor frequency, $\gamma|\mathbf{B}_0|$, from the RF frequency ω_{RF}:

$$\Delta\omega_0 \equiv \gamma|\mathbf{B}_0| - \omega_{RF}. \qquad [1]$$

1090-7807/01 $35.00

The second frequency, ω_1, measures the amplitude of the RF pulse and is defined by

$$\gamma B_{1c}(t) = \omega_1 \cos(\omega_{RF} t + \varphi), \quad [2]$$

where B_{1c} is the circularly polarized component of the RF field $\mathbf{B}_1$ that is perpendicular to $\mathbf{B}_0$. The nutation frequency during an RF pulse is given by $\Omega = \sqrt{\omega_1^2 + \Delta\omega_0^2}$.

We analyze the spin dynamics in the local rotating frame that rotates around $\mathbf{B}_0(\mathbf{r})$ with frequency ω_{RF}. The coordinate system in this rotating frame is chosen at each point $\mathbf{r}$ such that the $\hat{z}$ axis is pointing along the local $\mathbf{B}_0$ field and the $\hat{x}$ axis is pointing along the local direction of $\mathbf{B}_{1c}$ when $\varphi = 0$. We make the usual transformation:

$$M_{+1} \equiv M_x + iM_y \quad [3]$$

$$M_{-1} \equiv M_x - iM_y \quad [4]$$

$$M_0 \equiv M_z. \quad [5]$$

With these variables, the evolution under free precession has only diagonal elements:

$$\begin{pmatrix} M_{+1}(t) \\ M_{-1}(t) \\ M_0(t) \end{pmatrix} = \begin{pmatrix} e^{i\Delta\omega_0 t} & 0 & 0 \\ 0 & e^{-i\Delta\omega_0 t} & 0 \\ 0 & 0 & 1 \end{pmatrix} \begin{pmatrix} M_{+1}(0) \\ M_{-1}(0) \\ M_0(0) \end{pmatrix}. \quad [6]$$

Radiofrequency pulses mix in general all the elements:

$$\begin{pmatrix} M_{+1}(t_p) \\ M_{-1}(t_p) \\ M_0(t_p) \end{pmatrix} = \begin{pmatrix} \Lambda_{+1,+1} & \Lambda_{+1,-1} & \Lambda_{+1,0} \\ \Lambda_{-1,+1} & \Lambda_{-1,-1} & \Lambda_{-1,0} \\ \Lambda_{0,+1} & \Lambda_{0,-1} & \Lambda_{0,0} \end{pmatrix} \begin{pmatrix} M_{+1}(0) \\ M_{-1}(0) \\ M_0(0) \end{pmatrix}. \quad [7]$$

For RF pulses of phase φ and duration t_p, the matrix elements $\Lambda_{l,m}$ for an arbitrary frequency offset $\Delta\omega_0$ and RF field strength ω_1 are given by

$$\Lambda_{+1,+1} = \frac{1}{2}\left\{\left(\frac{\omega_1}{\Omega}\right)^2 + \left[1 + \left(\frac{\Delta\omega_0}{\Omega}\right)^2\right]\cos(\Omega t_p)\right\} + i\left(\frac{\Delta\omega_0}{\Omega}\right)\sin(\Omega t_p) \quad [8]$$

$$\Lambda_{-1,-1} = \frac{1}{2}\left\{\left(\frac{\omega_1}{\Omega}\right)^2 + \left[1 + \left(\frac{\Delta\omega_0}{\Omega}\right)^2\right]\cos(\Omega t_p)\right\} - i\left(\frac{\Delta\omega_0}{\Omega}\right)\sin(\Omega t_p) \quad [9]$$

$$\Lambda_{0,0} = \left(\frac{\Delta\omega_0}{\Omega}\right)^2 + \left(\frac{\omega_1}{\Omega}\right)^2 \cos(\Omega t_p) \quad [10]$$

$$\Lambda_{+1,0} = \frac{\omega_1}{\Omega}\left\{\frac{\Delta\omega_0}{\Omega}[1 - \cos(\Omega t_p)] - i\sin(\Omega t_p)\right\} e^{+i\varphi} \quad [11]$$

$$\Lambda_{-1,0} = \frac{\omega_1}{\Omega}\left\{\frac{\Delta\omega_0}{\Omega}[1 - \cos(\Omega t_p)] + i\sin(\Omega t_p)\right\} e^{-i\varphi} \quad [12]$$

$$\Lambda_{0,+1} = \frac{1}{2}\frac{\omega_1}{\Omega}\left\{\frac{\Delta\omega_0}{\Omega}[1 - \cos(\Omega t_p)] - i\sin(\Omega t_p)\right\} e^{-i\varphi} \quad [13]$$

$$\Lambda_{0,-1} = \frac{1}{2}\frac{\omega_1}{\Omega}\left\{\frac{\Delta\omega_0}{\Omega}[1 - \cos(\Omega t_p)] + i\sin(\Omega t_p)\right\} e^{+i\varphi} \quad [14]$$

$$\Lambda_{+1,-1} = \frac{1}{2}\left(\frac{\omega_1}{\Omega}\right)^2 [1 - \cos(\Omega t_p)] e^{+i2\varphi} \quad [15]$$

$$\Lambda_{-1,+1} = \frac{1}{2}\left(\frac{\omega_1}{\Omega}\right)^2 [1 - \cos(\Omega t_p)] e^{-i2\varphi}. \quad [16]$$

Note that $\Lambda_{-l,-m} = \Lambda^*_{+l,+m}$. The matrix elements depend on the phase of the pulse, φ, as $\Lambda_{l,m} \sim e^{i(l-m)\varphi}$. This property is used to separate the different coherence pathways by phase cycling.

For the analysis of a sequence with N RF pulses, the evolution can be divided into different coherence pathways (*11*), labeled by $q_1, q_2, \ldots, q_N$. Here q_k denotes the coherence after the kth pulse and can be -1, 0, or $+1$. The spectrum for a given coherence pathways is calculated by

$$M_{q_1,q_2,\ldots,q_N} = \left(\prod_{k=1}^{N} \Lambda_{q_k,q_{k-1}}\right) \exp\{i\Delta\omega_0 \sum_{k=1}^{N} q_k t_k\}, \quad [17]$$

where $q_0 = 0$ when the system is assumed to be initially in thermal equilibrium. Here t_k is the time between the kth and $k+1$th pulse and $\Lambda_{q_k,q_{k-1}}$ are given by Eqs. [8] to [16] with the pulse amplitude, duration, and phase of the kth pulse. The magnetization following an N pulse sequence is the sum over all possible coherence pathways:

$$\mathbf{M}^{(N)} = \sum_{q_1,\ldots,q_{N-1}} \left[M_{q_1,\ldots,q_{N-1},0}\hat{z} + M_{q_1,\ldots,q_{N-1},+1}\left(\frac{\hat{x} - i\hat{y}}{2}\right) + M_{q_1,\ldots,q_{N-1},-1}\left(\frac{\hat{x} + i\hat{y}}{2}\right)\right]. \quad [18]$$

Taking advantage of the fact that $M_{-q_1,-q_2,\ldots,-q_N} = M^*_{q_1,q_2,\ldots,q_N}$, this can be rewritten as

$$\mathbf{M}^{(N)} = \sum_{q_1,\ldots,q_{N-1}} [\mathrm{Re}\{M_{q_1,\ldots,q_{N-1},+1}\}\hat{x} + \mathrm{Im}\{M_{q_1,\ldots,q_{N-1},+1}\}\hat{y} + \mathrm{Re}\{M_{q_1,\ldots,q_{N-1},0}\}\hat{z}]. \quad [19]$$

2.2. Diffusion

When spins diffuse in an inhomogeneous field during the free precession intervals, the accumulated phase for a given coherence pathway is not just $\Sigma_k\, q_k\Delta\omega_0 t_k$, but there is an additional contribution from random phases, $\Sigma_k\, q_k\phi_k$. During each interval, the random phase, ϕ_k, depends on the path integral of the spin in the field inhomogeneity. The effect of diffusion on the spin dynamics can be described by including in each coherence pathway a term of the form $\langle \exp\{i\ \Sigma_{k=1}^{N} q_k\phi_k\}\rangle_{\phi_1,\ldots,\phi_N}$ in Eq. [17]. It is important to take into account the correlations between the random phases in the different intervals before taking the average. For unrestricted diffusion in a constant gradient g, the diffusion terms are purely real. Following the approach of Woessner (*12*), the result for a general coherence pathway is given by

$$\langle \exp\{i \sum_{k=1}^{N} q_k\phi_k\}\rangle_{\phi_1,\ldots,\phi_N} = \exp\left\{-\gamma^2 g^2 D\left[\sum_{k=1}^{N}\frac{1}{3}q_k^2 t_k^3 + \sum_{k=1}^{N} q_k t_k \sum_{l=1}^{k} q_l t_l T_l + \sum_{k=1}^{N} q_k t_k (t_k + T_k)\sum_{l=k+1}^{N} q_l t_l\right]\right\}. \quad [20]$$

Here D is the diffusion coefficient of the fluid and T_k is the sum of all the durations of free precession from the first instance a nonzero coherence is created up to the beginning of the kth pulse.

Several smaller effects of diffusion have been neglected: (i) The gradient in the RF field strength, B_1, is assumed to be negligible. (ii) The effect of diffusion during the RF pulses has been ignored. (iii) Fluctuations in the nutation frequency Ω are ignored. These fluctuations are not important as long as the spins diffuse during the measurement a distance small compared to the slice thickness, $\sqrt{DT_{\mathrm{exp}}} \ll \omega_1/\gamma g$. In our experiments, this is always fulfilled.

If diffusion is restricted, the right-hand side of Eq. [20] is modified. For a few coherence pathways, such as the direct echoes and the stimulated echo, results for selected geometries can be found in (*13*), (*14*), and (*15*) and references therein.

2.3. Relaxation

Relaxation attenuates each coherence pathway with a time constant T_1 during the periods with $q_k = 0$ and with a time constant T_2 when $q_k = \pm 1$. This can be incorporated by including a term $\exp\{-\Sigma_{k=1}^{N}((q_k^2/T_2) + (1 - q_k^2)/T_1)t_k\}$ for each pathway. Relaxation and diffusion effects therefore modify the spectrum of a coherence pathway, Eq. [17], by

$$M_{q_1,q_2,\ldots,q_N} = \left(\prod_{k=1}^{N}\Lambda_{q_k,q_{k-1}}\right)\exp\{i\Delta\omega_0\sum_{k=1}^{N} q_k t_k\} \times \langle \exp\{i\sum_{k=1}^{N} q_k\phi_k\}\rangle \times \exp\left\{-\sum_{k=1}^{N}\left(\frac{q_k^2}{T_2} + \frac{1-q_k^2}{T_1}\right)t_k\right\}, \quad [21]$$

where $q_0 = 0$.

When T_1 relaxation is important, the total signal is not just given by the sum of all N-pulse coherences $\mathbf{M}^{(N)}$ in Eq. [19]. T_1 relaxation gives rise to extra M_0 magnetization after the free precession intervals that is then refocused by the later pulses. For the evaluation of the total magnetization, in addition to the N-pulse coherences, all $N - k$-pulse coherences ($k = 1, 2, \ldots, N - 1$) describing the last $N - k$ pulses have to be evaluated:

$$\mathbf{M} = \mathbf{M}^{(N)} + \sum_{k=1}^{N-1}(1 - \exp\{-t_k/T_1\})\mathbf{M}^{(N-k)} + (1 - \exp\{-t_N/T_1\})\hat{z}. \quad [22]$$

In the CPMG sequence discussed below, this complication is avoided by using phase cycling of the first pulse.

3. EXPERIMENTAL TECHNIQUES

Measurements have been performed in the fringefield of a Nalorac 2-T superconducting magnet with a horizontal bore of 30 cm. The sample is placed on-axis 50 cm outside the magnet. At this location, the field strength is 41.4 mT and the gradient is 132 mT/m. The RF coil consists of a 40-mm-diameter solenoid, tuned to the Larmor frequency of 1.764 MHz, and has a quality factor $Q = 13.4$.

The sample container consists of a long Teflon rod that sits vertically in the RF coil. Within this rod, the 2-cm-long cylindrical sample cell of 2 cm diameter is oriented horizontally along the gradient direction. The cell was filled with either NiCl doped water or tap water, and the relevant diffusion coefficient is $D = 2.3 \times 10^{-9}$ m^2/s.

An Apollo Tecmag spectrometer was used for the pulse generation and signal acquisition. The signal was acquired with a dwell time of 2 μs and later digitally filtered with a lowpass filter of bandwidth ± 100 kHz. This frequency interval includes the whole range of possible offset frequencies in our sample in the gradient field, $|\Delta\omega_0|/2\pi < 56$ kHz. The RF pulse amplitude

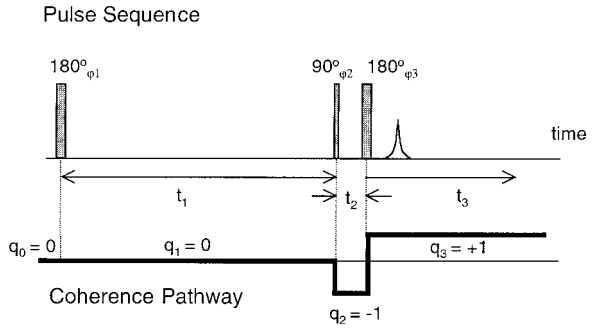

FIG. 1. Timing of the inversion-recovery pulse sequence is shown at the top and the desired coherence pathway is indicated at the bottom.

was adjusted to 235 μT, resulting in pulse durations $t_{180} = 2t_{90} = 50\ \mu s$. With these values, the normalized range of offset frequencies in our sample, $\Delta\omega_0/\omega_1$, is between ± 5.6. This is sufficiently large that the sample can be considered to be infinitely extended along the gradient direction. The bandwidth of the resonance circuit, $\omega_{RF}/Q = 2\pi \times 132$ kHz, is sufficient to avoid amplitude distortions of the signal. The dominant effect of the finite bandwidth is a small delay of the signal by $4Q/\omega_{RF} = 4.8\ \mu$s. This delay is the sum of two terms: the resonant circuit delays the RF pulses that the spins observe by $2Q/\omega_{RF}$ and then the voltage induced in the tuned coil is delayed by the same amount.

4. INVERSION RECOVERY

Two different pulse sequences have been tested experimentally and compared with the general theoretical analysis. The first sequence emphasizes the aspect of relaxation. Figure 1 shows the sequence of inversion recovery with echo detection. The desired pathway is $q_0 = 0 \rightarrow q_1 = 0 \rightarrow q_2 = -1 \rightarrow q_3 = +1$.

4.1. Phase Cycling

It is impossible to select a desired coherence pathway over a wide frequency range just by careful adjustment of the pulse duration. We use phase cycling to reduce the number of coherence pathways that can interfere with the desired signal. The phase cycling shown in Table 1 was derived from the phase dependence of $\Lambda_{q_k,q_{k-1}}$ in Eqs. [8] to [16]. To select the desired coherence pathway, the acquisition phase has to be set to $\varphi_{acq} = \sum_{k=1}^{N} (q_{k-1} - q_k)\varphi_k = \varphi_2 - 2\varphi_3$. Using this phase cycling, only the coherence pathways $(q_1, q_2, q_3) = (0, -1, +1)$ and $(q_2, q_3) = (-1, +1)$ contribute. All other contributions cancel. Note that it is impossible to separate the two remaining pathways by further phase cycling.

4.2. Echo Shape

With this phase cycling, the resulting spectrum of the transverse magnetization after the third pulse is calculated from Eqs. [21] and [22] for the two contributing coherence pathways and becomes

$$M_x + iM_y = \Lambda^{(3)}_{+1,-1}\Lambda^{(2)}_{-1,0} e^{i\Delta\omega_0(t_3-t_2)} - e^{-t_1/T_1}\Lambda^{(3)}_{+1,-1}\Lambda^{(2)}_{-1,0}(1 - \Lambda^{(1)}_{0,0}) e^{i\Delta\omega_0(t_3-t_2)}. \quad [23]$$

For clarity, we have suppressed the diffusion and T_2 relaxation terms for the t_2 and t_3 intervals. Each matrix element Λ is calculated for the parameters of the pulse indicated by the superscript. This expression shows that the echo shape depends on t_1/T_1. For perfect 90° and 180° pulses on resonance, Eq. [23] reduces to the familiar expression $1 - 2e^{-t_1/T_1}$. In Fig. 2, the signal measured for different values of recovery time t_1 is compared with the calculated signal obtained from Eq. [23] by integration over $\Delta\omega_0$. There is excellent agreement between measurement and calculation.

In both measurement and calculation, the echo is not centered at $t_3 = t_2$, but is delayed by at time Δt. This is a spin dynamics effect caused by the finite pulse width. The phase of one of the three matrix elements appearing in Eq. [23], $\Lambda_{-1,0}$, depends to first order on $\Delta\omega_0$. The echo amplitude peaks at a time when this phase is canceled by the phase factor $e^{i\Delta\omega_0(t_3-t_2)}$. This occurs at $t_3 = t_2 + \Delta t$, where

$$\Delta t = \frac{1 - \cos(\omega_1 t_{p2})}{\omega_1 \sin(\omega_1 t_{p2})}, \quad [24]$$

and t_{p2} is the duration of the second pulse. When this pulse is a nominal 90° pulse, the delay becomes $\Delta t = 2t_{90}/\pi$, in agreement with (*16*). In our measurements, this delay is 15.9 μs and exceeds the previously discussed electronic delay due to the finite response time of the resonant circuit, $4Q/\omega_{RF} = 4.8\ \mu$s.

4.3. Extraction of T_1

We present two different approaches to extract the relaxation time T_1 from the measurements in strongly inhomogeneous

TABLE 1
Eight-Step Phase Cycling Used for the Inversion-Recovery Experiment

Pulse phases			
φ_1	φ_2	φ_3	Acquisition phase
$+x$	$+x$	$+x$	$+x$
$+x$	$+y$	$+x$	$+y$
$+x$	$-x$	$+x$	$-x$
$+x$	$-y$	$+x$	$-y$
$+x$	$+x$	$-x$	$+x$
$+x$	$+y$	$-x$	$+y$
$+x$	$-x$	$-x$	$-x$
$+x$	$-y$	$-x$	$-y$

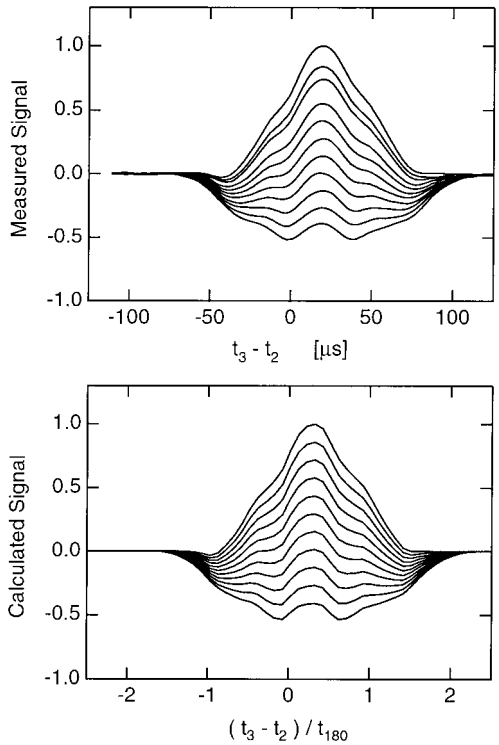

FIG. 2. Comparison of measured (top) and calculated (bottom) signals for the inversion-recovery sequence shown in Fig. 1. The sample is water, doped with NiCl with a nominal $T_1 = 110$ ms, and measured in the fringefield at 1.764 MHz. The measured echoes were recorded for $t_1 = 26$ μs, 10.5 ms, 22.3 ms, 36 ms, 51 ms, 69 ms, 92 ms, 120 ms, 180 ms, 230 ms, and 1 s. The other parameters are $t_2 = 159$ μs, $t_{180} = 50$ μs. For the calculated echoes shown in the bottom, it was assumed that $\exp\{-t_1/T_1\} = 0, 0.1, 0.2, \ldots, 1$.

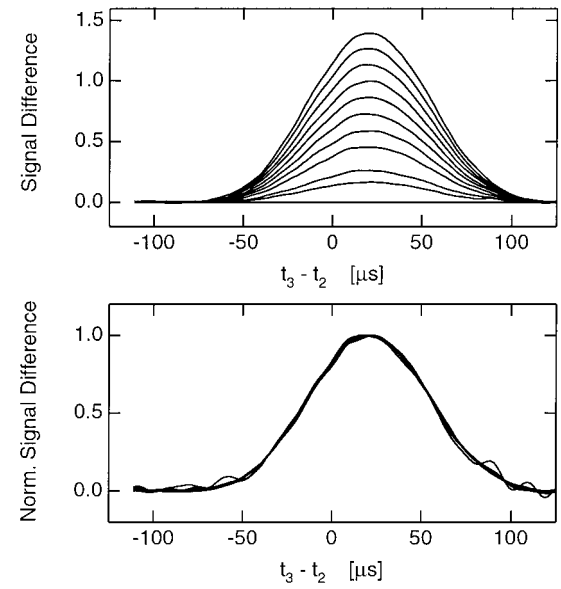

FIG. 4. Difference of the signal with $t_1^* = 1$ s $\gg T_1$, from signals with shorter values of t_1 (shown at the top of Fig. 2) versus time. At the bottom, each difference signal is normalized with respect to the amplitude at the echo peak. This demonstrates that the shapes of all difference echoes are identical.

fields. The first approach is based on the fact that the integral of the echo over the acquisition time corresponds to the on-resonance behavior. On resonance, the response is simply given by $1 - 2e^{-t_1/T_1}$. We can therefore extract the relaxation time from the areas of the measured spin echoes with an exponential fit. This is demonstrated in Fig. 3, using the data shown at the top of Fig. 2. This method requires an acquisition window long enough to capture all of the echo signal. Such a long integration window is not optimal for signal-to-noise reasons, but this is the consequence of only using the signal close to resonance.

The second approach does not have this limitation and is the superior method. It is based on the observation that the signal consists of the superposition of two terms as described in Eq. [23]. Only the second term depends on T_1 and on the recovery time t_1. Therefore, if we subtract signals acquired for two different recovery times, t_1 and t_1^*, the first term is eliminated. It is most convenient to subtract the signal with a long recovery time, $t_1^* \gg T_1$, from all of the other measurements. In this case, the difference signal is simply given by the second term of Eq. [23]: the amplitude of the difference signal is proportional to $\exp\{-t_1/T_1\}$ and its shape is independent of t_1 and T_1. In Fig. 4, this is demonstrated using the data from Fig. 2. The shape of

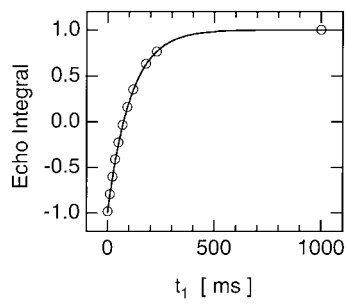

FIG. 3. Integral of the measured echoes over time t_3 versus delay t_1. The solid line is the fit of $1 - 2\exp\{-t_1/T_1\}$ to the data with $T_1 = 107$ ms.

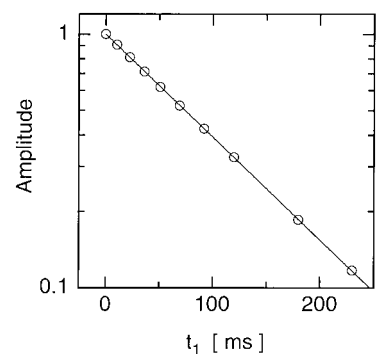

FIG. 5. Amplitude of the difference signal shown at the top of Fig. 4 versus recovery time, t_1. The straight line is a fit to the data with $T_1 = 107$ ms.

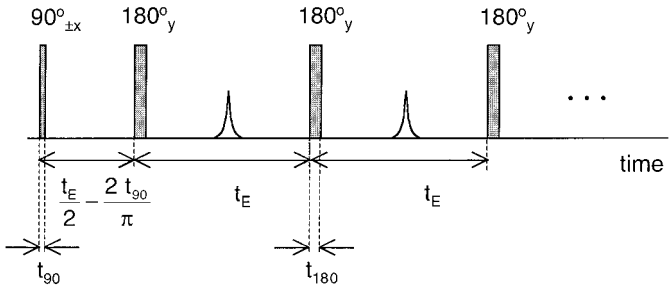

FIG. 6. Timing of the CPMG sequence used in the experiment. The spacing of the first two pulses is reduced to compensate for the finite pulse duration as explained in the text. In the experiments, 200 echoes were acquired with pulse durations $t_{180} = 2t_{90} = 50$ μs and with different echo spacings, t_E, between 0.40 and 23.85 ms.

the difference signal is indeed independent of recovery time, as shown at the bottom of Fig. 4. It is now straightforward to extract the amplitudes of the difference signal, preferably with a window function that is matched to the shape of the difference signal. The amplitudes follow the expected exponential decay as shown in Fig. 5. The extracted value for T_1 agrees with the previous determination that was based on the echo integrals. Note that this procedure is equally applicable if the strength of the RF is misset or if there is a distribution of B_1 values. The shape and overall amplitude of the difference echo will be affected, but not the time dependence of its amplitude. When the T_1 decay is characterized by more than a single relaxation time, the data can be analyzed using a multiexponential fitting routine. Examples of such fitting routines are given in (*17*) and references therein.

5. CARR–PURCELL–MEIBOOM–GILL SEQUENCE

5.1. Introduction

The Carr–Purcell–Meiboom–Gill sequence is widely used in well logging (*4, 9, 10*) and materials testing (*5*), where the magnetic fields are very inhomogeneous. Previous studies of the CPMG sequence in inhomogeneous fields (*9, 10*) have shown that the measured decay rate depends both on T_1 and T_2. Asymptotic expressions for the echo amplitude in the absence of diffusion were also obtained (*10*).

Here we concentrate on the diffusion effects of the CPMG sequence in a constant gradient. This has not been studied in detail beyond the first few echoes (*9, 10*). In well logging, diffusion effects have been commonly analyzed by assuming that the on-resonance behavior is an adequate approximation for the total signal decay (*18*). Our goal is to understand properly the off-resonance effects on diffusion.

The timing of the CPMG pulse sequence used in our experiment is shown in Fig. 6. The acquisition window is centered in the middle between subsequent 180° pulses and is 256 μs long. The initial echo spacing has been optimized to $t_E/2 - 2t_{90}/\pi$. This follows from the analysis leading to Eq. [24] above. This timing maximizes the signal and ensures that all echoes form half way between the 180° pulses. Measurements were taken with 21 different echo spacings t_E ranging from 400 μs to 23.85 ms. For all values of t_E, 200 echoes were acquired. For the shortest echo spacing, diffusive attenuation is negligible even for the 200th echo, whereas for the longest echo spacing, the first echo is already attenuated by more than an order of magnitude. We use a simple two-step phase cycling: the phase of the initial 90° pulse and of the acquisition is alternated between $\pm x$ without changing the phase of the 180° pulse. In addition, standard CYCLOPS phase cycling was used. The sample is tap water with a measured $T_1 = T_2 = 2.3$ s. In our measurements, relaxation is therefore only a minor effect.

In Fig. 7, measurements of the first 10 echoes are displayed for 8 different echo spacings. For the longer echo spacings, diffusion both reduces the echo amplitudes and changes the shape of the echoes. For the shortest echo spacing of 400 μs, diffusion is not significant. In this case, the shape of the echo

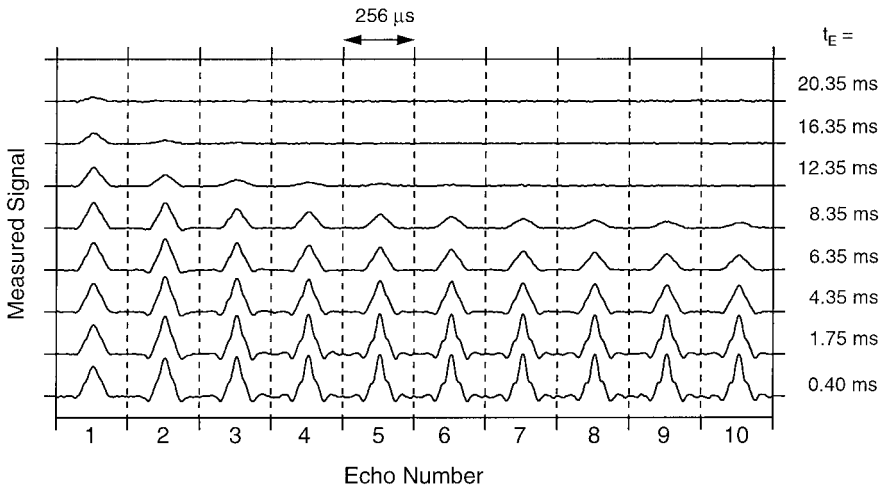

FIG. 7. Measurement of the first 10 echoes of the CPMG sequence with a water sample for the echo spacings t_E indicated on the right. All echoes are on the same scale, but offset from each other.

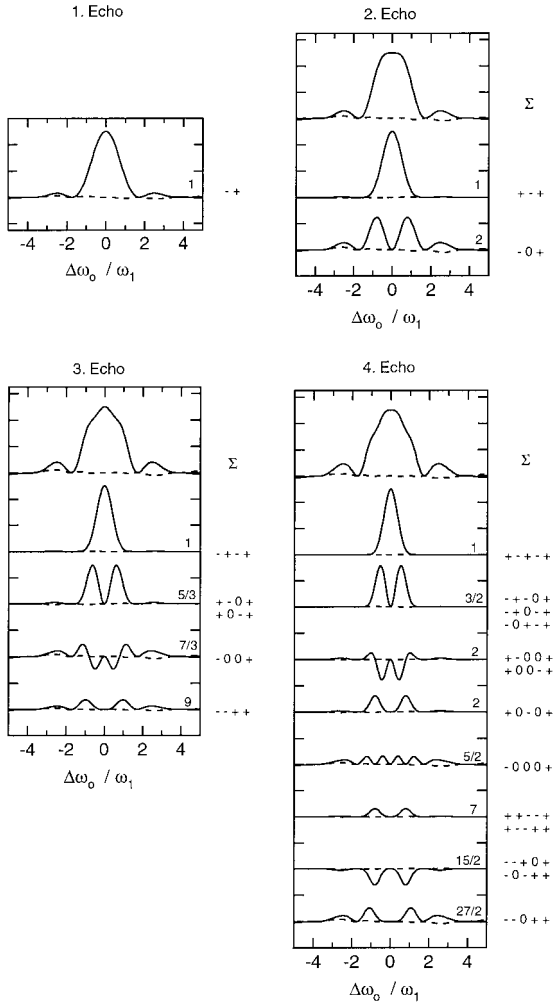

FIG. 8. The spectra of all the coherence pathways that contribute to the first four echoes are plotted versus the normalized offset frequency, $\Delta\omega_0/\omega_1$. The solid line shows the *y* channel; the dashed line shows the *x* channel. Each spectrum is labeled on the right with the coherence pathway $(q_1, \ldots, q_N)$. For the second to fourth echoes, the top spectrum labeled by Σ is the sum of all spectra that contribute to this echo. The number listed with each spectrum is $\eta_l^{(N)}$, the normalized decay rate for unrestricted diffusion defined in Eq. [26].

is rapidly approaching an asymptotic form independent of echo number.

5.2. Spectrum and Echo Shapes

For a quantitative comparison of the data with theory, we have to consider all coherence pathways that contribute to the CPMG echoes and evaluate the spectrum and the diffusive attenuation.

With the standard phase cycling for the CPMG, the signal after the *N*th pulse consists of the superposition of all *N*-pulse coherence pathways that start with $q_1 = \pm 1$ and end with $q_N = +1$. The phase cycling eliminates the second and third terms of Eq. [22]. A coherence will only contribute significantly to an echo at $t = Nt_E$ if the dominant phase factor $\Delta\omega_0 \sum_{k=1}^{N} q_k t_k$ in Eq. [17] vanishes. For the CPMG sequence, this condition becomes

$$q_1 + 2\sum_{k=2}^{N-1} q_k + q_N = 0. \qquad [25]$$

Figure 8 shows the spectra $M_{q_1,\ldots,q_{N=+1}} = \Pi_{k=1}^{N} \Lambda_{q_k,q_{k-1}}$ of all the coherence pathways that fulfill Eq. [25] for the first four echoes. On resonance, only the direct echoes contribute. With the timing adjustment of the first pulse spacing, the spectra of all relevant coherence pathways are almost purely in the *y*-channel. In a constant gradient, the echo shape is therefore nearly symmetric in the time domain.

For higher echo numbers, the number of possible coherence pathways contributing to a given echo increases exponentially. For $N = 15$, there are over 10^6 such pathways. When diffusion and relaxation are negligible, the signal is given by the sum over all these coherence pathways. As shown in Fig. 8, it is remarkable that this sum changes very little from echo to echo, even though the individual spectra for the coherence pathways change significantly. The experiments for short echo spacings shown in Fig. 7 confirm this observation. An explanation can be found in Ref. (*10*), where the CPMG was analyzed in terms of effective rotations.

Under diffusion, each coherence pathway will decay with a different decay rate that is given by Eq. [20] for unrestricted diffusion. The rates depend only through the combination $g^2Dt_E^3$ on the gradient, diffusion coefficient, and echo spacing. It is therefore convenient to introduce a normalized diffusion decay rate, $\eta_l^{(N)}$, for the *l*th coherence pathway $(q_1^{(l)}, \ldots, q_N^{(l)})$ of the *N*th echo. This is analogous to the approach in Ref. (*6*).

$$\exp\left\{-\frac{1}{12}\eta_l^{(N)}\gamma^2 g^2 D t_E^3 N\right\} \equiv \langle \exp\{i\sum_{k=1}^{N} q_k^{(l)}\phi_k\}\rangle_{\phi_1,\ldots,\phi_N} \qquad [26]$$

The values of $\eta_l^{(N)}$ are indicated in Fig. 8 for each coherence pathway. The pathways with contributions far off-resonance are in general attenuated faster than pathways with contributions close to resonance.

Using Eqs. [18], [21], and [20], we have calculated the total spectra of the first 15 echoes for the echo spacings used in the experiment by summing the contributions over all possible coherence pathways. The measured signal corresponds to the Fourier transform of the calculated spectrum. In Fig. 9, a representative sample of measured echoes are compared with calculations. The agreement is excellent.

In these plots, the origin of the time axis corresponds to the midpoint between two subsequent 180° pulses. With our modified spacing between the first two pulses, all echoes form close to the midpoint between the pulses. Under close inspection, the measurements show the constant delay of 4.8 μs caused by the

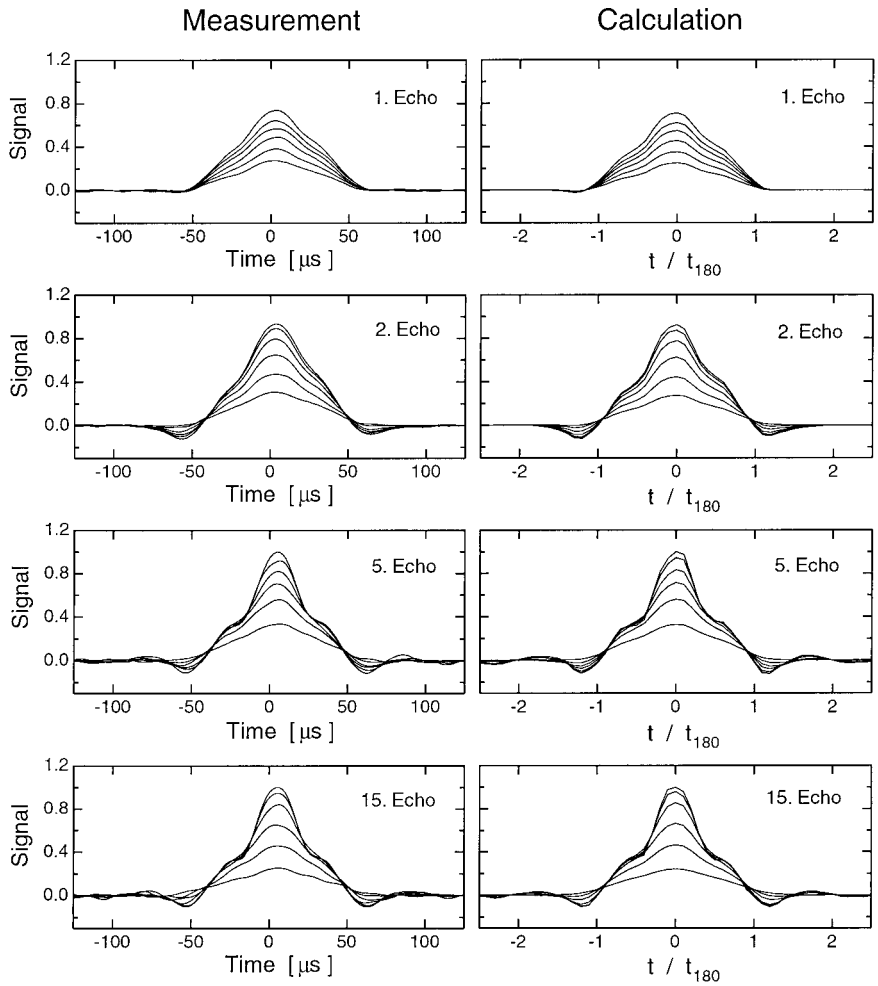

FIG. 9. Comparison of measured and calculated echoes of the CPMG sequence for the 1st, 2nd, 5th, and 15th echoes in a constant gradient. For the 1st echo, t_E = 0.4, 8.35, 10.35, 12.35, 14.35, 16.35 ms; for the 2nd echo, t_E = 0.4, 4.35, 6.35, 8.35, 10.35, 12.35 ms; for the 5th echo t_E = 0.4, 2.35, 3.75, 4.95, 6.35, 8.35 ms; for the 15th echo t_E = 0.4, 1.35, 2.75, 3.75, 4.95, 6.35 ms, respectively. The vertical scale is identical for all graphs. In the measurements, t_{180} = 50 μs.

resonance circuit, as discussed before. The echoes are nearly symmetric in time, confirming that the out-of-phase contributions to the spectra are small.

The first echo is roughly triangular. The later echoes develop distinct shoulders and oscillations before and after the peak. For the longer echo spacings, these features are quickly attenuated by diffusion. This is more evident in Fig. 10, where the echoes of Fig. 9 are replotted, normalized with respect to the peak value.

Unlike the later echoes, the shape of the first echo is not affected by diffusion. The reason is that this echo is formed by a single coherence pathway, as shown in Fig. 8. In contrast, the shapes of the later echoes broaden, and the shoulders and oscillations vanish as the contributions from the higher coherence pathways decay first. Ultimately, the shape will be determined by the mode with the slowest decay, the direct echo, whose width scales like $\sqrt{N}$ for large N. This limiting echo shape is shown as a dashed line on the right-hand side of Fig. 10. With sufficient signal-to-noise ratio, it is possible to extract diffusion information directly from the shape of a single echo. For $T_1 = T_2$, relaxation only attenuates the signal amplitude without affecting the shape of the echo. In this case, it is in principle possible to extract separately diffusion and relaxation information from CPMG measurements using a single value of t_E.

5.3. *Diffusion Attenuation of Echo Amplitude*

The results in Fig. 10 imply that the measured decay rate due to diffusion depends on the detection bandwidth (*9*). In the extreme limit when a very narrow bandwidth is used, off-resonance effects are irrelevant. The decay is then expected to follow the familiar form of $\exp\{-(1/12)\gamma^2 g^2 D t_E^3 N\}$. We have confirmed this with our data. A narrow bandwidth is obtained by integrating each echo over a time interval that is much longer than t_{180}. In our experiments, the acquisition window for each echo is just over $5t_{180}$ long. In Fig. 11, we plot the integrals of the measured signal over the whole acquisition

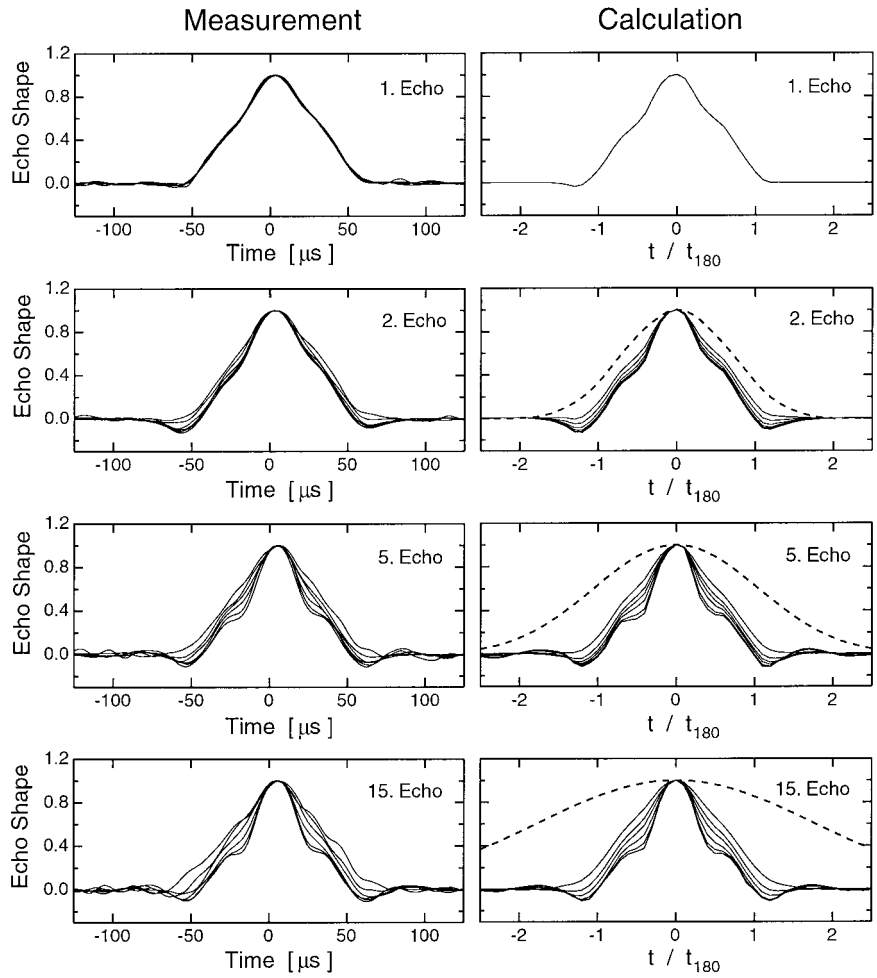

FIG. 10. Comparison of measured and calculated echo shapes versus time. The data are the same as in Fig. 9 but each echo is normalized with respect to its peak value. The dashed lines indicate the asymptotic echo shapes when only the contribution of the direct echo (with least diffusive attenuation) remains.

window versus $\gamma^2 g^2 D t_E^3 N/12$. Within experimental error, the measurements collapse onto a single line that coincides with the expected on-resonance decay. In Fig. 11, we have corrected for the small decay due to relaxation, $\exp\{-Nt_E/T_2\}$.

When a different window function is used to improve for instance the signal-to-noise ratio of the extracted amplitudes, other coherence paths contribute and a nonexponential decay will be observed. With a general window function, $w(t)$, the extracted echo amplitude from the measured signal of the Nth echo, $s_N(t)$, is given by

$$A^{(N)} = \frac{\int dt\, s_N(t) w(t)}{[\int dt\, w(t) w^*(t)]^{1/2}}. \qquad [27]$$

The echo amplitude $A^{(N)}$ has in general contributions from many different coherence pathways l. To highlight the effect of diffusion, we factor out the diffusive decay and write $A^{(N)}$ as

$$A^{(N)} = \sum_l a_l^{(N)} \exp\left\{-\eta_l^{(N)} \frac{1}{12} \gamma^2 g^2 D t_E^3 N\right\}. \qquad [28]$$

The amplitude $a_l^{(N)}$ characterizing the contribution from a particular pathway $(q_1, \ldots, q_N)$ is independent of diffusion but depends on the window function. It can be calculated from the spectrum of this coherence pathway, $M_{q_1,\ldots,q_N}(\Delta\omega_0)$ defined by Eq. [17], and the Fourier transform of the window function, $\tilde{w}(\Delta\omega_0)$:

$$a_l^{(N)} = \frac{\int d\Delta\omega_0\, M_{q_1,\ldots,q_N}(\Delta\omega_0) \tilde{w}(\Delta\omega_0)}{[\int d\Delta\omega_0\, \tilde{w}(\Delta\omega_0) \tilde{w}^*(\Delta\omega_0)]^{1/2}}. \qquad [29]$$

For optimal signal-to-noise ratio, the signal should be analyzed with a filter that matches the expected signal shape, $w(t) = \langle s_N^*(t) \rangle$. This is difficult to implement in practice, because the expected signal shape varies from echo to echo and depends on the diffusion coefficient. The diffusion coefficient of the sample is often unknown and a quantity to be measured. For this reason, we propose to use the shape of the asymptotic echo in the absence of diffusive attenuation as a near optimal window function for all echoes. This shape depends only on the pulse width and can be calculated from the simple asymp-

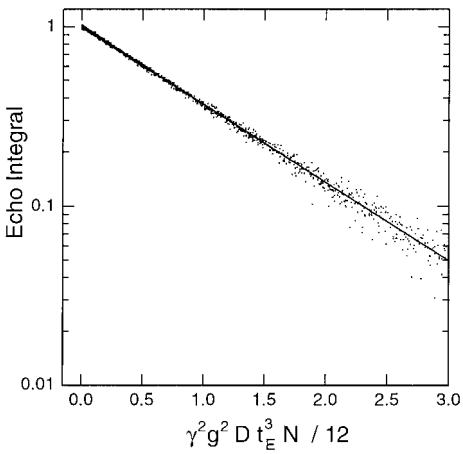

FIG. 11. Integrals of the measured echoes over the total acquisition window versus $(1/12)\gamma^2 g^2 D t_E^3 N$. Within experimental error, the integrals of all 200 echoes and 21 echo spacings fall onto the on-resonance decay curve, shown as a solid line.

totic expression given in Ref. (*10*), or alternatively, it can be determined experimentally from measurements with short echo spacing.

The calculated amplitudes, $a_l^{(N)}$, for this window function are plotted in Fig. 12 as a function of the normalized decay rate, $\eta_l^{(N)}$, for the first 15 echoes. The information presented in Fig. 12 is sufficient to calculate the expected echo amplitude for any value of gradient, diffusion coefficient, or echo spacing through Eq. [28]. The first echo has only a contribution from a single coherence path, but with increasing echo number N, the number of contributing coherences increases very rapidly. The contribution from the direct echo pathway with $\eta = 1$ decreases as more complicated pathways with higher decay rates start to contribute. For a given echo number, the normalized decay rates are bounded by $1 \leq \eta_l^{(N)} \leq N^2$. The amplitudes tend to be a maximum near $\eta \simeq 1$ and tend to decrease for higher η. Note that some of the amplitudes $a_l^{(N)}$ are negative. The dependence of the contributions for the first three coherence pathways versus echo number is shown in Fig. 13. The first coherence pathway corresponds to the standard echo on resonance. In the second and third coherence pathways, the magnetization is stored along the z direction for one or two consecutive echo spacings, respectively, otherwise the RF pulses act as refocusing pulses (see Fig. 8). The sum of all amplitudes $\Sigma_l a_l^{(N)}$ for a given echo is nearly independent of N after the third echo; the fluctuations are less than 0.25%. This is consistent with the earlier observation that in the absence of diffusion; the echoes quickly approach an asymptotic limit (*10*).

In Fig. 14, we plot the experimental echo amplitudes, extracted from the measured signal by filtering it with the asymptotic echo shape without diffusion, versus the dimensionless quantity $(1/12)\gamma^2 g^2 D t_E^3 N$. The echo amplitudes have been corrected for the small T_1, T_2 decay, as discussed before. We observe again excellent agreement between experiment and

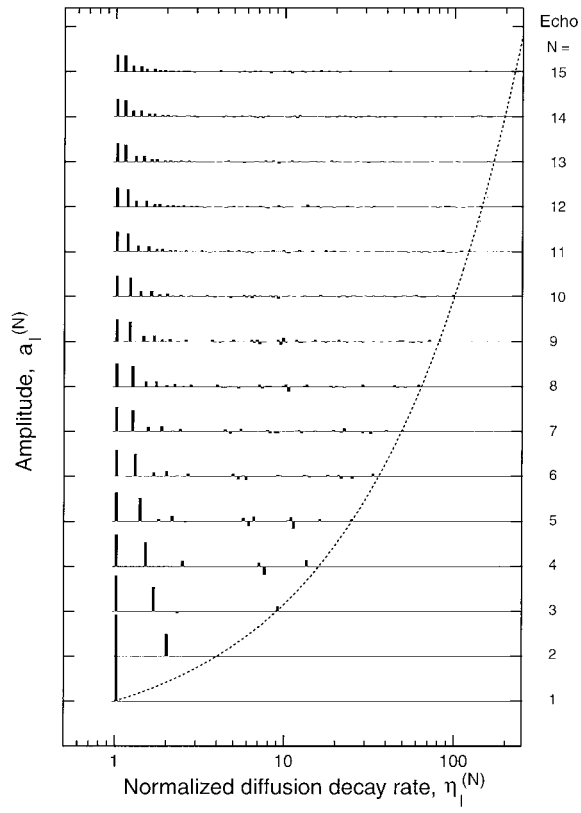

FIG. 12. Calculated amplitudes, $a_l^{(N)}$, versus the normalized decay rate, $\eta_l^{(N)}$, for the first 15 echoes as given by Eq. [28]. The window function $w(t)$ was chosen to be the asymptotic echo shape in absence of diffusion. The distributions are plotted on the same vertical scale, but offset from each other. The dashed line shows an upper bound for the decay rate, $\eta_l^{(N)} \leq N^2$.

theory. The first echo decays exponentially with the on-resonance decay rate of the direct echo. The overall amplitude is reduced because the window function used is not matched to the first echo. The amplitude decays of the second and higher echoes are clearly multiexponential.

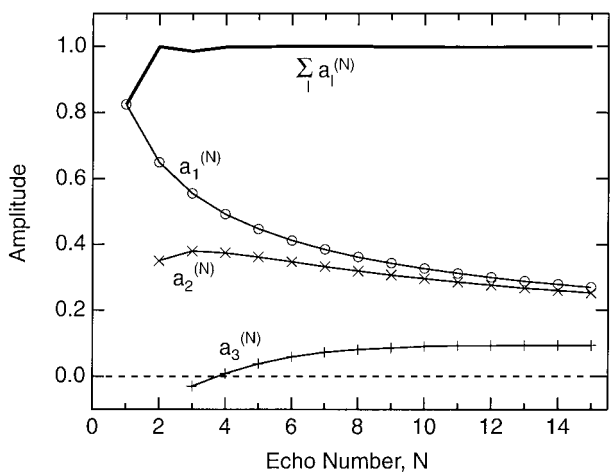

FIG. 13. Amplitude $a_l^{(N)}$ of the contributions by the first three coherence pathways to the echo amplitude versus echo number N. Also shown is the sum of all amplitudes that contribute to a given echo, $\Sigma_l a_l^{(N)}$, versus echo number.

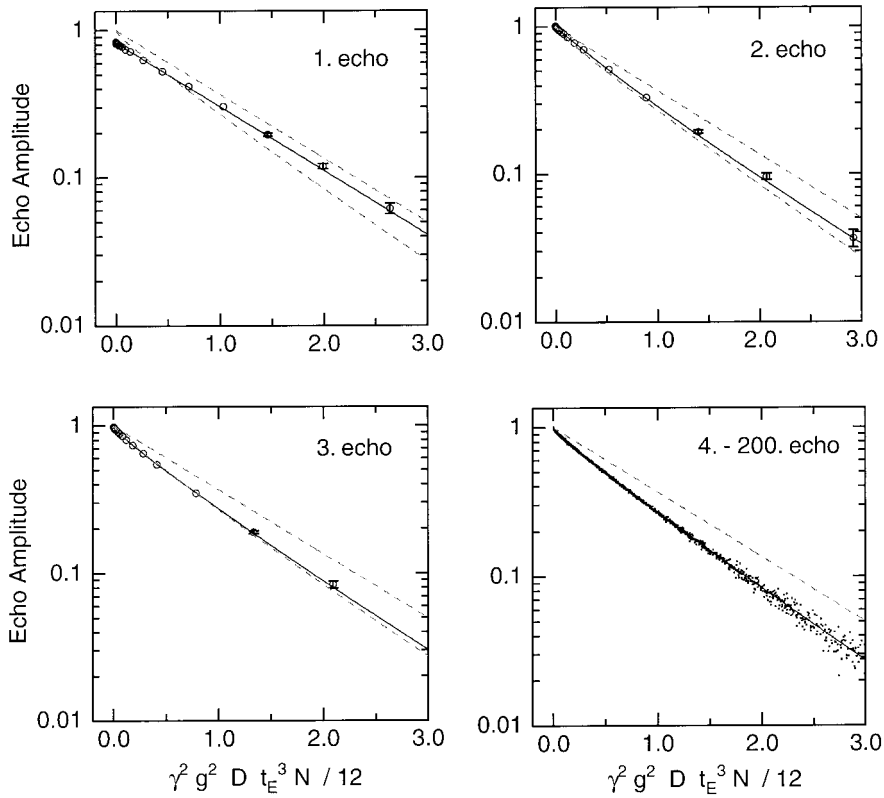

FIG. 14. Echo amplitude versus $(1/12)\gamma^2 g^2 D t_E^3 N$ for the CPMG sequence and unrestricted diffusion. The circles and dots are the experimental points obtained by filtering the measured echoes using the asymptotic echo shape in the absence of diffusion. The solid lines show the theoretical calculations with no adjustable parameters. The upper dashed line shows the expected on-resonance behavior. The lower dashed line shows the theoretical curve for $N = 15$. The first echo amplitude decays exponentially with a rate identical to the on-resonance case whereas the higher echo amplitudes have a distinctly nonexponential decay. After the third echo, the echo amplitudes collapse onto a single line within experimental error.

The calculated decay curves for the 4th to 15th echoes are almost indistinguishable, the predicted amplitudes deviate from each other by less than 6% over the displayed range. The experimental results for the 4th to 200th echoes are all plotted on the same graph in Fig. 14. Within experimental uncertainty, all the data collapse onto a single line that is identical to the calculated decay for the 15th echo. This was not anticipated. It indicates that even though the decay for the higher echoes shows a strong deviation from the on-resonance behavior, it still depends only through the combination $g^2 D t_E^3 N$ on gradient strength, diffusion coefficient, echo spacing, and echo number. This implies that with increasing N, the distributions shown in Fig. 12 will not change significantly anymore. It will approach a continuous asymptotic distribution with a maximum close to $\eta = 1$ and a tail extending to larger values of η. With the present theoretical approach, it is difficult to verify this directly by numerical calculations. The calculations cannot be extended to much higher values of N, because the number of possible coherence pathways diverges.

The amplitudes $a_l^{(N)}$ shown in Fig. 12 were calculated for a fixed value of the B_1 field. When the B_1 field over the sample is characterized by a distribution of B_1 values, these amplitudes will change, but not the normalized decay rates, $\eta_l^{(N)}$. In this case, the asymptotic shape of the echo amplitude decay in Fig. 14 has to be redetermined for the particular experimental condition. It is also common to encounter samples with multiple components that have different diffusion coefficients. It is possible to extract the diffusion coefficients by fitting the CPMG decay to a multiparameter function, similar to the usual multiexponential fits (*17*). However, in this case, the exponential kernel function has to be replaced by the asymptotic decay shown in the bottom right panel of Fig. 14.

6. CONCLUSION

The excellent agreements between calculated and measured responses in Sections 4 and 5 demonstrate that the theory presented in Section 2 accurately describes the spin dynamics in inhomogeneous fields, including diffusion and relaxation effects. This approach is based on dividing the signal into contributions from all possible coherence pathways. We have shown that changes in the phase of the RF pulses only change the overall phase of the spectrum of each coherence pathway. In grossly inhomogeneous fields, phase cycling therefore remains an effective means to select desired coherence pathways. It is useful to isolate specific coherence pathways, because the attenuation caused by diffusion and relaxation is uniform across the spectrum of a given coherence pathway, but in

general different from one pathway to the next. If a single coherence pathway is isolated, relaxation and diffusion do not affect the shape of the signal, only its amplitude. The relevant parameters can then be extracted quantitatively from the decay of the measured amplitudes. With a single coherence pathway, the decay is independent of detection bandwidth. This approach was demonstrated for the case of inversion recovery in Figs. 4 and 5.

In the analysis of this sequence, we have also studied the effect of finite pulse width on the timing of the echo formation. It was shown that the echo is delayed by some time Δt given by Eq. [24]. This time can be reinterpreted in the following way: The period of free precession following a 90° pulse does not start at the end of the pulse, but effectively at a time $2t_{90}/\pi$ earlier. For this reason, the first pulse spacing in the CPMG sequence has to be reduced by the same amount.

In the CPMG sequence, many coherence pathways contribute. It would be in principle possible to devise a phase cycling scheme that selects contributions from only a few coherence pathways at each echo. However, this would require a large number of phase cycles and therefore a long acquisition time. In addition, it would lead to a signal reduction, because the different coherence pathways mainly interfere constructively at the time of the echo. The superposition of many coherence pathways complicates the calculation of diffusion effects. As expected, in this case diffusion does not only change the amplitude, but also the shape of the higher echoes. We are able to calculate the shape in details for up to 15 echoes and get excellent agreement with the measurements. Echo amplitudes have been extracted using as filter the asymptotic echo shape without diffusion. We find that the echo decay due to diffusion in a fringefield of constant gradient g is faster than given by the familiar form of $\exp\{-(1/12)\gamma^2 g^2 D t_E^3 N\}$. This is caused by signal coming from regions away from the center of the excited slice where contributions from other coherence pathways decay faster than the on-resonance signal. More surprisingly, we found both experimentally and numerically that to a good approximation, the diffusion decay still scales with $\gamma^2 g^2 D t_E^3 N$ for $N > 3$. This implies that in inhomogeneous fields, it is still possible to extract the diffusion coefficient from the amplitude decay of CPMG measurements with different echo spacings. However, the decay has to be analyzed with a kernel that is not simply a single exponential, but with a multiexponential function corresponding to the asymptotic distribution in Fig. 12. The exact shape of the kernel depends on the filter used to extract the echo amplitudes.

This analysis of the CPMG sequence in terms of coherence pathway complements an earlier analysis of the CPMG (*10*) that is based on the evaluation of the eigenvectors $\hat{n}$ of the refocusing cycle. The present analysis is able to take account of diffusion effects, but is limited to a relatively small number of echoes. The approach in (*10*) can be used to calculate the signal for an arbitrary number of pulses, but it is not able to include diffusion effects.

ACKNOWLEDGMENT

I thank U. Scheven for his help in getting the experimental setup running.

REFERENCES

1. P. J. McDonald, Stray field magnetic resonance imaging, *Prog. Nucl. Magn. Reson. Spectrosc.* **30,** 69–99 (1997).
2. R. Kimmich, W. Unrath, G. Schnur, and E. Rommel, NMR measurement of small self-diffusion coefficients in the fringe field of superconducting magnets, *J. Magn. Reson.* **91,** 136–140 (1991).
3. R. Kimmich and E. Fischer, One- and two-dimensional pulse sequences for diffusion experiments in the fringe field of superconducting magnets, *J. Magn. Reson. A* **106,** 229–235 (1994).
4. R. L. Kleinberg, Well logging, *in* "Encyclopedia of Nuclear Magnetic Resonance," Vol. 8, pp. 4960–4969, Wiley, Chichester, 1996.
5. G. Eidmann, R. Savelsberg, P. Blümler, and B. Blümich, The NMR MOUSE, a mobile universal surface explorer, *J. Magn. Reson. A* **122,** 104–109 (1996).
6. R. Kaiser, E. Bartholdi, and R. R. Ernst, Diffusion and field-gradient effects in NMR Fourier spectroscopy, *J. Chem. Phys.* **60,** 2966–2979 (1974).
7. A. Sodickson and D. G. Cory, A generalized *k*-space formalism for treating the spatial aspects of a variety of NMR experiments, *Prog. NMR Spectrosc.* **33,** 77–108 (1998).
8. T. B. Benson and P. J. McDonald, The application of spin echoes to stray-field imaging, *J. Magn. Reson. B* **109,** 314–317 (1995).
9. G. Goelman and M. G. Prammer, The CPMG pulse sequence in strong magnetic field gradients with applications to oil-well logging, *J. Magn. Reson. A* **113,** 11–18 (1995).
10. M. D. Hürlimann and D. D. Griffin, Spin dynamics of Carr–Purcell–Meiboom–Gill-like sequences in grossly inhomogeneous B_0 and B_1fields and application to NMR well logging, *J. Magn. Reson.* **143,** 120–135 (2000).
11. Richard R. Ernst, Geoffrey Bodenhausen, and Alexander Wokaun, "Principles of Nuclear Magnetic Resonance in One and Two Dimensions," Clarendon Press, Oxford, 1987.
12. D. E. Woessner, Effects of diffusion in nuclear magnetic resonance spin-echo experiments, *J. Chem. Phys.* **34,** 2057–2061 (1961).
13. P. Linse and O. Söderman, The validity of the short-gradient-pulse approximation in NMR studies of restricted diffusion. Simulations of molecules diffusing between planes, in cylinders and spheres, *J. Magn. Reson. A* **116,** 77–86 (1995).
14. P. N. Sen, A. André, and S. Axelrod, Spin echoes of nuclear magnetization diffusing in a constant magnetic field gradient and in a restricted geometry, *J. Chem. Phys.* **111,** 6548–6555 (1999).
15. S. L. Codd and P. T. Callaghan, Spin echo analysis of restricted diffusion under generalized gradient waveforms: Planar, cylindrical, and spherical pores with wall relaxivity, *J. Magn. Reson.* **137,** 358–372 (1999).
16. C. P. Slichter, "Principles of Magnetic Resonance," third ed., pp. 39–45, Springer-Verlag, Berlin, 1996.
17. G. C. Borgia, R. J. S. Brown, and P. Fantazzini, Uniform-penalty inversion of multiexponential decay data, *J. Magn. Reson.* **132,** 65–77 (1998).
18. R. Akkurt, H. J. Vinegar, P. N. Tutunjian, and A. J. Guillory, NMR logging of natural gas reservoirs, *in* "Trans. SPWLA 36th Annual Logging Symposium, Paris," 1995.